Emergence of Invar effect with excellent mechanical property by electronic structure modulation in LaFe$_{11.6-x}$Co$_x$Si$_{1.4}$ magnetocaloric materials

Hou-Bo Zhou [a,b,1], Zi-Bing Yu [a,b,1], Feng-xia Hu [a,b,c,*], Jian-Tao Wang [a,b,c,*], Fei-Ran Shen [d], Jia-Zheng Hao [d], Lun-Hua He [c,d], Qing-Zhen Huang [e], Yi-Hong Gao [a,b], Bing-Jie Wang [a,b], Zhuo Yin [a,b], Zheng-Ying Tian [a,b], Jing Wang [a,b,*], Yun-Zhong Chen [a,b], Ji-Rong Sun [a,b,c], Tong-Yun Zhao [a,g], Bao-Gen Shen [a,b,f,g,*]

[a] Beijing National Laboratory for Condensed Matter Physics, Institute of Physics, Chinese Academy of Sciences, Beijing 100190, PR China
[b] School of Physical Sciences, University of Chinese Academy of Sciences, Beijing 101408, PR China
[c] Songshan Lake Materials Laboratory, Dongguan, Guangdong 523808, PR China
[d] Spallation Neutron Source Science Center, Dongguan, Guangdong 523803, PR China
[e] NIST Center for Neutron Research, National Institute of Standards and Technology, Gaithersburg, MD 20899, USA
[f] Ningbo Institute of Materials Technology & Engineering, Chinese Academy of Sciences, Ningbo, Zhejiang 315201, China
[g] Ganjiang Innovation Academy, Chinese Academy of Sciences, Ganzhou, Jiangxi 341000, China

ARTICLE INFO

ABSTRACT

Materials with Invar effect, i.e. zero thermal expansion (ZTE), have important applications in precision manufacturing. Here we report the emergence of Invar effect with excellent mechanical property by modulating electronic structure in LaFe$_{11.6-x}$Co$_x$Si$_{1.4}$, a family known for magnetocaloric effect. The observed linear thermal expansion coefficient ($\alpha_l \sim 1.5 \times 10^{-8}$ K^{-1}, 5–250 K, by XRD; $\alpha_l \sim 2.7 \times 10^{-7}$ K^{-1}, 109–250 K, by dilatometer) is superior to most other ZTE materials including the famous Invar alloy Fe$_{0.65}$Ni$_{0.35}$. By taking advantage of distinct resolution ability of neutrons and X-rays to Fe/Co adjacent elements, the site occupancy of Co atoms was determined by joint refinements of neutron powder diffraction (NPD) and X-ray diffraction (XRD). On the basis, *ab initio* calculations were performed on the atomically resolved electronic band structure. The incorporation of Co atoms alters the electron transfer properties by increasing 3d bonding electrons at Co sub-lattice, as a result, spontaneous magnetostriction is inhibited and Invar effect prevails in the ferromagnetic region of LaFe$_{10.6-}$Co$_{1.0}$Si$_{1.4}$. The electron local function (ELF) evidences the enhanced bonding strength and origin of excellent mechanical properties. The measured compressive strength can be up to ~340 MPa, which endows the LaFe$_{10.6}$Co$_{1.0}$Si$_{1.4}$ good machining ability. Further, the mode-mode coupling coefficient *b* calculated from density of states (DOS) explains the evolution of phase transition order with Co doping, which gives LaFe$_{10.6}$Co$_{1.0}$Si$_{1.4}$ a significant advantage in its effective cooling capacity under low magnetic fields. The present study provides a solid foundation for exploiting multifunctional application of La(Fe,Si)$_{13}$ alloys with Co incorporation from the perspective of electronic structure modulation.

1. Introduction

Most materials expand on heating due to anharmonic lattice vibration, resulting in positive thermal expansion (PTE). To meet the demands of precision industry, abnormal thermal expansion (ATE), including zero thermal expansion (ZTE) and negative thermal expansion (NTE), has become one of the current focuses in materials science [1–19]. In the past years, great efforts have made with many materials being identified showing useful ATE. The reported NTE materials include ZrW$_2$O$_8$ family [3], PbTiO$_3$-based compounds [4], CuO nanoparticles [5], (Bi,La)NiO$_3$ [6,7], ScF$_3$ [8], antiperovskite manganese nitrides [11,12], and La(Fe,Co,Si)$_{13}$ compounds [13]. While ZTE

---

materials include $Zr_{1-x}Sn_xMo_2O_8$ [14], $Fe_{0.65}Ni_{0.35}$ [15], YbGaGe [16] and the very recently reported $Mn_{1-x}Ni_xCoSi$ [17], $Ho_2(Fe,Co)_{17}$ [10, 18], and $Hf_{0.85}Ta_{0.15}Fe_2C_{0.01}$ Kagome magnets [19]. Particularly, Cao et al reported ultrawide temperature range super-Invar behavior in $Ho_2Fe_{16}Co$ [10]. The dominated mechanism includes phonon-driven and electron-driven categories, while the latter contains electronic transition type such as magnetic, ferroelectric, or charge order.

On the other hand, magnetic refrigeration based on magnetocaloric effect (MCE) has attracted an increasing attention for its environmental-friendly and energy-saving superiority compared to conventional vapor compression technique [20–24]. A common feature of giant MCE materials is the strong spin-lattice coupling, and a number of MCE materials with magnetostructural/magnetoelastic transition exhibit abnormal lattice expansion, which provides an ideal platform for exploring NTE or ZTE materials. La(Fe,Si)$_{13}$-based compounds with NaZn$_{13}$-type structure are well known for MCE [21,25–27]. The concurrent magnetic transition and negative lattice expansion lead to giant MCE, which has attracted tremendous attentions aiming at magnetic refrigeration application since its first report in 2001 [21,25–27]. To be as ATE materials, giant NTE was reported in La(Fe,Si,Co)$_{13}$ compounds in 2013 [13]. Later, ZTE was observed in a broad temperature interval (20–275 K) in LaFe$_{11.0}$Si$_{2.0}$H$_\delta$ hydrides [28]. However, the effect of inevitable hydrogen decrepitation makes the hydrides extremely brittle and naturally break into powders, seriously limiting its application. In contrast, Co regulation can produce great advantages, including the adjustments of phase transition temperature, ATE, and mechanical properties.

Here we report the emergence of Invar effect with excellent mechanical property by electronic structure modulation via Co doping in LaFe$_{11.6-x}$Co$_x$Si$_{1.4}$ magnetocaloric materials. Although the Co-doped La(Fe,Si)$_{13}$ alloys have already been used as magnetic refrigerants for years [26,27], the underlying mechanism tuning physical properties is unclear. The dilemma rooted in the fact that, despite over 20 years of attention upon this material family, the occupancy of Co atoms in La(Fe, Si,Co)$_{13}$ remains uncertain. In this work, by taking advantage of the different resolution ability of neutrons and X-rays to Fe/Co adjacent elements, the occupancy information of Co atoms in La(Fe,Si,Co)$_{13}$, i.e. LaFe$_{11.6-x}$Co$_x$Si$_{1.4}$, was determined by utilizing a joint refinement strategy of neutron powder diffraction (NPD) and X-ray diffraction (XRD). On the basis, *ab initio* calculations were performed on the atomically resolved electronic band structure. The results indicated that the incorporation of Co atoms alters the electron transfer properties. After the entry of the Co atoms into the lattice, the increase of the non-bonding states in the majority spin channel can be compensated by the depopulation of other non-bonding states upon magnetic ordering, leading to an increase of 3d bonding electrons at Co sub-lattice, which inhibits the spontaneous magnetostriction and weakens the lattice stress. Combined with the benefits from significantly enhanced effective exchange coupling parameter (J_{eff}) upon Co doping, Invar effect was demonstrated over a wide temperature interval in the ferromagnetic region of LaFe$_{10.6}$Co$_{1.0}$Si$_{1.4}$. The observed linear thermal expansion coefficient ($\alpha_l \sim 1.5 \times 10^{-8}$ K^{-1}, $\Delta T = 5$–250 K) is better than most other ZTE materials [29–31] including the famous Invar alloy $Fe_{0.65}Ni_{0.35}$ ($\alpha_l \sim 1.5 \times 10^{-6}$ K^{-1}, 193–373 K) [15]. Moreover, the calculations of electron local function (ELF) show a higher degree of electron localization between Fe and Co atoms, which further explain the enhanced bonding strength and excellent mechanical properties in LaFe$_{10.6}$-Co$_{1.0}$Si$_{1.4}$ compared to LaFe$_{11.6}$Si$_{1.4}$. The measured compressive strength can be up to $\sim$340 MPa for LaFe$_{10.6}$Co$_{1.0}$Si$_{1.4}$ cuboids, which endows the materials good machining ability. Further, the correlation of electronic structure with phase transition nature was studied in detail. The mode-mode coupling coefficient b calculated from density of states (DOS) quantitatively explains the evolution from first-order phase transition (FOPT) to second-order phase transition (SOPT) upon Co doping. The elimination of hysteresis gives LaFe$_{10.6}$Co$_{1.0}$Si$_{1.4}$ a significant advantage in its effective cooling capacity under a low magnetic field by permanent magnets. The present study provides a solid foundation for the multifunctional application of La(Fe,Si)$_{13}$ alloys with Co incorporation. The findings pave the way for exploiting thermal-expansion-control engineering and related functional materials from the perspective of electronic structure modulation.

2. Experimental and computational details

LaFe$_{11.6-x}$Co$_x$Si$_{1.4}$ ($x = 0$, 1.0, hereafter denoted as Co0 and Co1, respectively) compounds were prepared by arc-melting technique. The as-cast ingots were then annealed at 1323 K for 40 days before quenching into liquid nitrogen. The crystal structure and thermal expansion were characterized by X-ray diffraction (XRD, Rigaku Smartlab) using a Cu-Kα target ($\lambda = 1.5406$ angstrom) equipped with a low-temperature chamber providing variable temperature within 5–300 K and a high-temperature chamber up to 1200 °C. Magnetic properties were measured by SQUID-VSM. The thermal expansion behaviors were also measured by an advanced thermo-dilatometer (NETZSCH DIL402).

By taking advantage of distinct resolution ability of neutrons and X-rays to Fe/Co adjacent elements, the joint refinement of neutron powder diffraction (NPD) and XRD was adopted to disclose the occupying information of Fe, Co, Si atoms in LaFe$_{11.6-x}$Co$_x$Si$_{1.4}$ (space group: Fm-3c). When X-rays interact with matters to produce scattering, the extra-nuclear electrons become the main scattering center in the atoms, and the scattering intensity increases with atomic number by linear correlation. Note that the coherent scattering lengths for Fe and Co are very close, i.e. 0.73 fm and 0.76 fm, respectively [32]. This leads to weak resolution ability and merges Fe/Co into almost the same element in the XRD patterns. In other words, Fe/Co atoms cannot be identified by XRD and the both appear the same. By utilizing the blinding character by XRD on Fe and Co atoms, we first determined the Si content by XRD in LaFe$_{11.6-x}$Co$_x$Si$_{1.4}$. Then NPD was employed to distinguish the two neighbor elements Fe and Co noting that the coherent scattering length by neutron is notably distinct for Fe and Co, which are 10.1 fm and 2.49 fm, respectively. Compared to X-ray, neutron mainly interacts with the nucleus to generate isotropic scattering, and the scattering intensity correlates nonlinearly with the atomic number. Hence neutron diffraction is able to identify neighbor elements and small atoms. In this work, NPD measurements were carried out by "Time-of-Flight" General Purpose Powder Diffractometer (GPPD) of China Spallation Neutron Source (CSNS), which provide users with a designed bandwidth 4.8 Å based on the neutron source of decoupled poisoned hydrogen moderator. The diffractometer uses the wavelength shifting scintillator neutron detector modules (4 × 4 mm2 Pixel) and covers 0.05 Å< d < 50.48 Å with gradually changing resolution (best resolution of 0.149% at high intensity mode) for the bandwidth 4.8 Å (0.1 - 4.9 Å, 4 - 8.8 Å, see details in Ref. [33]). And the wavelength band of the neutrons used for our measurement is 0.1 – 4.9 Å, which is sufficient for measuring and analyzing crystal structure, atomic occupancy, and magnetic structure. The full-profile Rietveld refinements of XRD and NPD patterns were performed by GSAS software.

First-principles calculations were based on the Korringa-Kohn-Rostocker (KKR) band structure method for ordered and chemically disordered alloys and Local Spin Density Approximation. We use 608 k-point in irreducible wadge of the Brillouin zone and spherical harmonic expansion up to $I_{max} = 3$ (spd-basis). Density functional theory (DFT) calculations are performed using the Vienna *ab initio* simulation package [34] with the all-electron projector augmented wave method [35]. The spin-polarized generalized gradient approximation (GGA) revised by Hammer *et al.* (RPBE) [36] was used as the exchange-correlation functional. The valence states $5s^25p^65d^16s^2$ for La, $3s^23p^2$ for Si, $3d^74s^1$ for Fe, and $3d^84s^1$ for Co are used with the energy cutoff of 500 eV for the plane wave basis set. A 2 × 2 × 2 supercell was constructed with the input of experimental lattice parameter $a\sim1.1528$ nm and the atomic occupation information from NPD and XRD joint refinements. The effective exchange coupling parameter J_{eff} were calculated using magnetic force theorem as implemented in KKR formalism. The

Brillouin-zone sampling is performed using a $3 \times 3 \times 3$ k-point grid for the total energy and electron localization function (ELF) calculations. The electronic density of states (DOS) are calculated using the Gaussian smearing with a broadening energy of 0.1 eV and 5000 of grid points on which the DOS is evaluated.

3. Results and discussion

3.1. Structure, Invar effect and mechanical properties

The refined XRD patterns (supplementary information Fig. S1) confirmed the phase-purity and $NaZn_{13}$-type crystallographic information for both Co0 and Co1 specimens. Fig. 1a shows the temperature dependent magnetization (M-T) of the two specimens under 0.01 T magnetic field. With Co introduction, a dramatic increase of the magnetic ordering temperature, i.e., Curie temperature (T_C), from 198 K (Co0) to 305 K (Co1) can be observed, as well as a slight decrease of saturation magnetization at 5 K (from 176.8 emu/g to 168.7 emu/g, see the inset in Figs. 1a and S2). Fig. 1b and c show the variable temperature XRD contour plots of Co0 and Co1, respectively, from 5 to 300 K. As the temperature rises across the T_C, the (531), (620) peaks show abrupt shift to higher 2θ for both Co0 and Co1, indicating a sudden contraction of lattice while the latter is smaller than the former. In the PM region above the T_C, the (531), (620) peaks move slightly to the low 2θ side with increased temperature for both Co0 and Co1, which corresponds to conventional PTE caused by anharmonic lattice vibration. The distinct difference between Co0 and Co1 appears in the ferromagnetic (FM) region. For Co0, below $T_C \sim 198$ K, the (531), (620) reflections of the FM phase shift slowly to high 2θ on heating, implying weak negative lattice thermal expansion in the FM region (5–190 K, Fig. 1d). In contrast, for Co1, the feature reflections of (531) and (620) in the FM region remain almost fixed with temperature below 250 K (Fig. 1c), suggesting ultra-low thermal expansion in the FM region.

In detail, Fig. 1d shows the temperature dependent lattice volume V for the two specimens refined from XRD patterns. One can note that with increasing temperature the V of Co0 shrinks slowly until T_C and then shows a sharp drop by $\Delta V/V \sim 1.2\%$. The corresponding linear coefficient of thermal expansion (CTE) is calculated to be $\alpha_l \sim -2.9 \times 10^{-6}$ K^{-1} within FM region below ~ 150 K, showing NTE behavior. With the introduction of Co, the contraction during phase transition becomes smaller, and NTE in the FM region flattened out. For Co1, the $\Delta V/V$ during phase transition reduces to $\sim 0.8\%$ around T_C, while the linear CTE decreases to $\alpha_l \sim 1.5 \times 10^{-8}$ K^{-1} in a broadened temperature region of $\Delta T \sim 250$ K (5~250 K), which is superior to most reported other ZTE materials and even the famous Invar alloy $Fe_{0.65}Ni_{0.35}$ (see Table S1, $\alpha_l \sim 1.5 \times 10^{-6}$ K^{-1}, 193–373 K). The temperature interval of ZTE for Co1 extends to low temperature covering the liquid nitrogen, liquid hydrogen, and even liquid helium temperature, making the materials more conducive in low-temperature precision manufacturing. Additionally, the linear thermal expansion curves ($\Delta L/L0$) were also measured by an thermo-dilatometer, the average linear expansion coefficient of Co1 ($LaFe_{10.6}Co_{1.0}Si_{1.4}$) is about $\alpha_l \sim 2.7 \times 10^{-7}$ K^{-1} (109K-
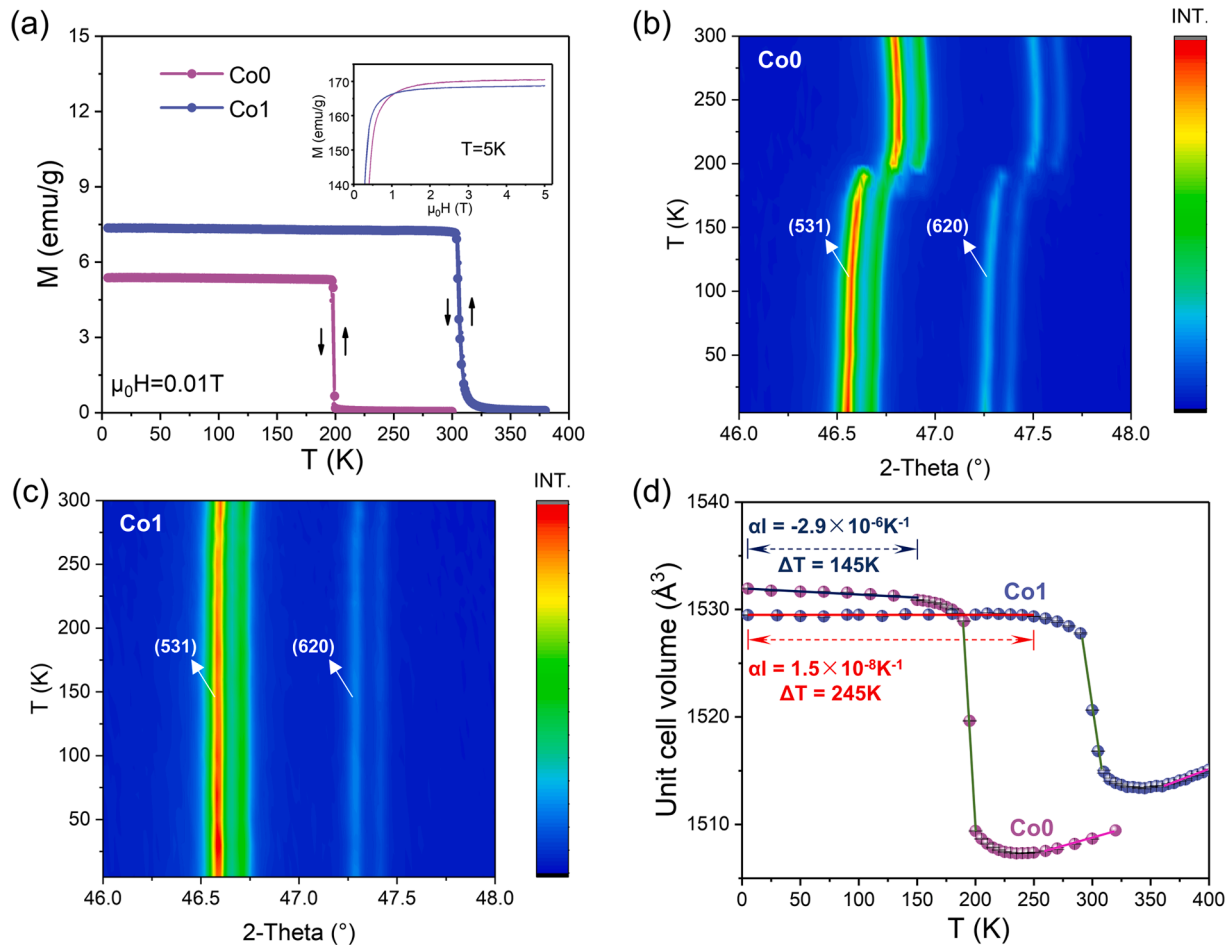

Fig. 1. (a) Temperature dependence of magnetization for $LaFe_{11.6-x}Co_xSi_{1.4}$ ($x = 0, 1.0$) under 0.01 T on heating and cooling. Inset shows the M-H curves at 5 K for the two specimens. Contour plots of the variable temperature XRD patterns of $LaFe_{11.6-x}Co_xSi_{1.4}$ for (b) Co0 and (c) Co1, where the (531) and (620) feature reflections are marked by white arrows. (d) The lattice volume vs. temperature for Co0 and Co1, where the linear CTEs α_l and the corresponding working intervals ΔT are marked.

250 K), which confirms the excellent ZTE property of our sample (Fig. S3). Compression tests were performed for Co1, as shown in Fig. 2. The mechanic strength is up to 340 MPa, hence machinable ZTE alloy can be realized in $LaFe_{11.6-x}Co_xSi_{1.4}$ ($x = 1.0$) compounds. In contrast, $LaFe_{11.6-x}Co_xSi_{1.4}$ ($x = 0$) without Co (Co0) show poor mechanical properties and naturally break into powders (see inset of Fig. 2).

3.2. Fe, Co, Si occupations determined by XRD and NPD joint refinements

In the ideal compound $LaFe_{13}$ with $NaZn_{13}$-type structure (see Fig. 3a), Fe atoms occupy two different Wycko-positions FeI (8b) and FeII (96i) in a ratio of 1:12. La and FeI atoms form the CsCl structure in a unit cell that includes eight molecular formula $LaFe_{13}$ [37]. Each FeII atom is surrounded by nine FeII nearest neighbors and one FeI atom, and twelve FeII atoms make up the icosahedron where the FeI atom locates at the center (see the thin gray enclosed in Fig. 3a). However, the exact occupation of introduced Co in the $NaZn_{13}$ lattice remains unclear since the discovery of $La(Fe,Co,Si)_{13}$ MCE materials more than 20 years ago. In other words, whether the Co atoms preferentially occupy 96i-site or randomly occupy 8b- and 96i- sites was not determined though the atomic number at 96i-site is 12 times more than that at 8b-site [38–40]. In $La(Fe,Co,Si)_{13}$, the 3 elements of Fe, Co and Si all occupy 2 sites of Fe. More than two unknown degrees of freedom in the same crystallographic position will lead to non-convergence during Rietveld refinement of occupancy. This is an insurmountable obstacle to resolve Co occupation by single means of either XRD or NPD, although neutrons have the ability to distinguish Fe/Co neighbors.

By taking advantage of distinct resolution ability of neutrons and X-rays to Fe and Co atoms, joint refinement by XRD and NPD was adopted to disclose the occupation information of Co dopants. Note that Co element locates at the eighth group of the fourth period (atomic radius $r_{Co} = 1.67$ Å) and adjacent to Fe ($r_{Fe} = 1.72$ Å), while Si ($r_{Si} = 1.46$ Å) locates at the fourth main group of the third period. The coherent scattering length for Fe and Co by X-ray is nearly the same, which is 0.73 fm and 0.76 fm, respectively [32]. This leads to weak resolution ability on neighbor Fe and Co elements by XRD. In this case, it is reasonable to consider Fe and Co as the same element. Therefore, the refinement of XRD pattern for $LaFe_{10.6}Co_{1.0}Si_{1.4}$ can be separated into two situations, i. e., $LaFe_{11.6}Si_{1.4}$ and $LaCo_{11.6}Si_{1.4}$ (Fig. S4-S5, Table S2). The refined occupancies of Fe/Si atoms for the two situations are shown in Table 1. Si atoms almost uniformly occupy 8b and 96i sites, and the corresponding occupancies are refined to be 11.84%(8b)/10.33%(96i) and 11.79%(8b)/10.33%(96i), equivalent to $LaFe_{11.64}Si_{1.36}$ and $LaCo_{11.65}Si_{1.35}$, respectively, well consistent with the nominal compositions.
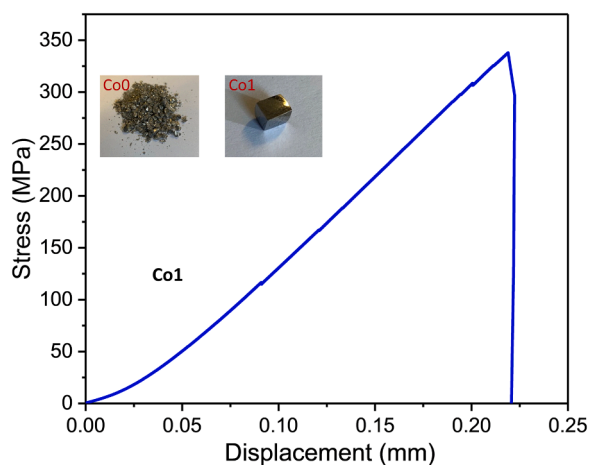

Fig. 2. Compressive stress-strain curve of Co1. Inset shows the physical snapshots of Co0 and Co1.

On the other hand, neutrons show a natural advantage identifying the neighbors Fe and Co, noting that the coherent scattering length for Fe and Co are 10.1 fm and 2.49 fm, respectively [32]. After the Si occupancies were determined by XRD, NPD was employed to distinguish Fe and Co (Figs. 3c, S6, Table S3). The Co occupancies are calculated to be 9.80% and 7.52% at 8b and 96i sites, respectively. The Co atoms at 8b-site are slightly higher than those at 96i site, implying that the doped Co atoms preferentially occupy the body center positions of the icosahedrons. These provide us with a basis for in-depth study of the physical property evolution by Co modulation.

3.3. Modulated electronic structure by Co-doping

The ZTE properties of metallic magnetic materials are mostly dominated by spontaneous magnetostriction because the volume change is closely relevant to spontaneous magnetic ordering in FM region. In addition, the consistent temperature intervals of ATE and ferromagnetism (Fig. 1a and 1d) indicate a strong coupling between the magnetic ordering and lattice thermal expansion. To explore the underlying mechanism of the magnetic ordering induced ATE in $LaFe_{11.6-x}Co_xSi_{1.4}$, *ab initio* calculations were conducted to study electronic band structures of both Co0 and Co1 in ferromagnetic-ordered (FM) and magnetic-disordered (PM) states. The magnetic disorder in the PM state was simulated using the disordered local moments (DLM) approach. Based on the atomic occupation from joint refinement of XRD and NPD, we calculated atomically resolved density of states (DOS) curves of the Fe- and Co-sub-lattices that occupying 8b and 96i sites, respectively, for the two specimens. Typically, Fig. 4a and b show comparatively the DOS curves at 96i site of the Fe sub-lattice for Co0 and the Co sub-lattice for Co1 (DOS curves for Fe-8b sub-lattice of Co0, and these for Fe-8b, Co-8b, Fe-96i sub-lattices of Co1 are shown in supplementary information Fig. S7). The magnetic disorder-to-order transition causes obvious differences in the DOS. In the DLM state of Co0 and Co1, the width of DOS curves extend smoothly across the Fermi level E_F for both Fe-96i (Co0) and Co-96i (Co1) sub-lattices (Fig. 4a and b). While in the FM state, E_F locates near the top energy of majority bands for the two sub-lattices. The almost fully occupied majority band implies a higher local magnetic moment of both the Fe and Co sub-lattices at FM state. Moreover, from DLM to FM state, a splitting of the electron bands was observed (Fig. 4a and b), which provides the valence electrons with extra kinetic energy. The increase in kinetic energy can be partially offset by the increase in lattice volume [41,42], implying a tendency for lattice to expand upon magnetic ordering.

Near the Fermi level E_F, the main contribution to DOS is the d-d hybridization between 3d electrons at 8b and 96i sites, which produces non-bonding and bonding orbitals in the majority and minority bands, respectively (as indicated in Fig. 4a and b) [43]. While below energy position of ~ -2 eV, fully filled d electrons in both the spin up and spin down channels appear as bonding states, and the spins of bonding electrons in the two channels cancel out each other. The difference between the number of electrons in the majority and minority, i.e., the non-bonding electrons, provide the atomic magnetic moment. By integrating the DOS curves, we found that the decrease of Co1 spin down channel from DLM to FM ($DLM_{spin\ down} = 3.3$, $FM_{spin\ down} = 2.8$, decreased by 0.5 electrons/atom) is relatively less than that of Co0 ($DLM_{spin\ down} = 2.7$, $FM_{spin\ down} = 1.9$, decreased by 0.8 electrons/atom), indicating increased bonding electrons and enhanced 3d metallic bond in Co1 compared with that of Co0.

Generally, less itinerant electrons are necessary for magnetism, and electron spins are arranged by exchange interactions. This exchange interaction does not work well when electrons are flowing. Volume expansion reduces the overlap of electronic orbitals, hence reducing the flow of electrons. Therefore, the system expands volume to assist magnetism when magnetic order occurs, which is described as a magnetic induced stress on the lattice [10], i.e. the spontaneous magnetostriction, which is closely related to the origin of metallic magnetism
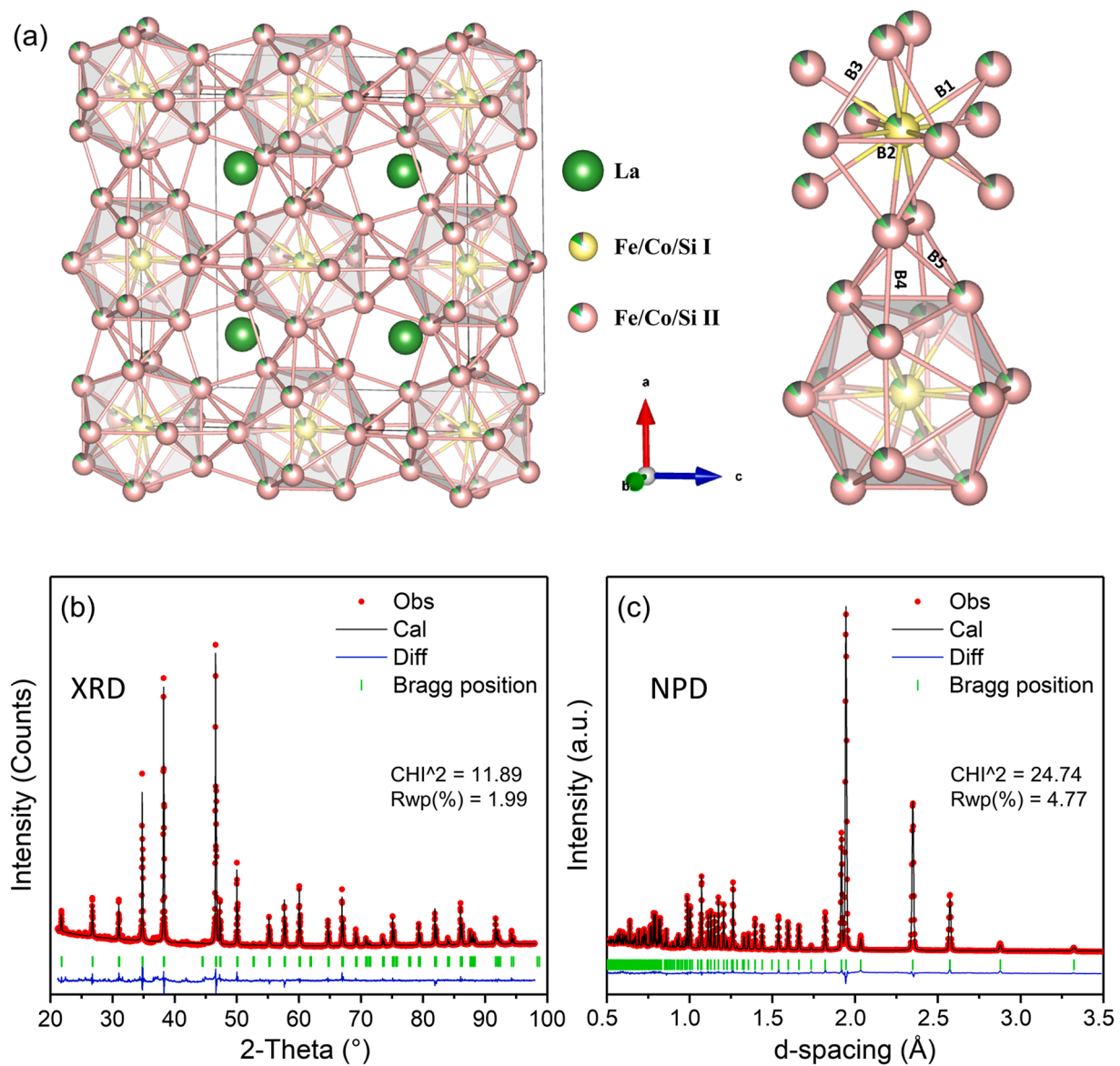
Fig. 3. (a) Three-dimensional structure of LaFe$_{11.6-x}$Co$_x$Si$_{1.4}$ ($x = 0$, 1.0) and the schematic view of the five Fe−Fe bonds, where the Fe−Fe bonds intra-icosahedrons (B1, B2, and B3) and between the icosahedrons (B4, B5) are marked. Rietveld refinement of (b) neutron powder diffraction (NPD) and (c) X-ray diffraction (XRD) patterns collected at room temperature for Co1. The observed (red dots), calculated patterns (black line), their difference (blue line), peak positions (green bar), error factors wRp and χ^2 are provided.

Table 1
The atomic occupancies of Fe/Co/Si at 8b and 96i site for LaFe$_{10.6}$Co$_{1.0}$Si$_{1.4}$ obtained by joint refinements of XRD and NPD patterns.

Diffraction type	Cases	Wyckoff position	Fe Frac. (%)	Co Frac. (%)	Si Frac. (%)	Refined composition
XRD	LaFe$_{11.6}$Si$_{1.4}$	8b (I)	88.16	–	11.84	LaFe$_{11.64}$Si$_{1.36}$
		96i (II)	89.67	–	10.33	
	LaCo$_{11.6}$Si$_{1.4}$	8b (I)	–	88.21	11.79	LaCo$_{11.65}$Si$_{1.35}$
		96i (II)	–	89.67	10.33	
NPD	LaFe$_{10.6}$Co$_{1.0}$Si$_{1.4}$	8b (I)	78.38	9.80	11.82	LaFe$_{10.64}$Co$_{1.0}$Si$_{1.36}$
		96i (II)	82.15	7.52	10.33	

[44]. Therefore, for Co0, the change in Fe-DOS from DLM to FM is primary ascribed to the depopulation of the bonding states in the minority band channel and the increase of the non-bonding states in the majority spin channel upon magnetic ordering (as indicated by the brown arrow in Fig. 4a). This fact leads to the weakening of metallic 3d bonds and the expansion of the interatomic distance, i.e., lattice stress induced by magnetic ordering, which, combining the band splitting mentioned above, produces the NTE in FM region for Co0 [41,44].

Whereas for Co1, the increased population of the non-bonding states can be compensated by the depopulation of other non-bonding states at higher energy position in the majority spin channel with the transition from DLM to PM (as indicated by the brown arrow in Fig. 4b). The above behaviors of the DOS curves for Co0 and Co1 are consistent with the electron transfer features obtained by integration, that is, the number of
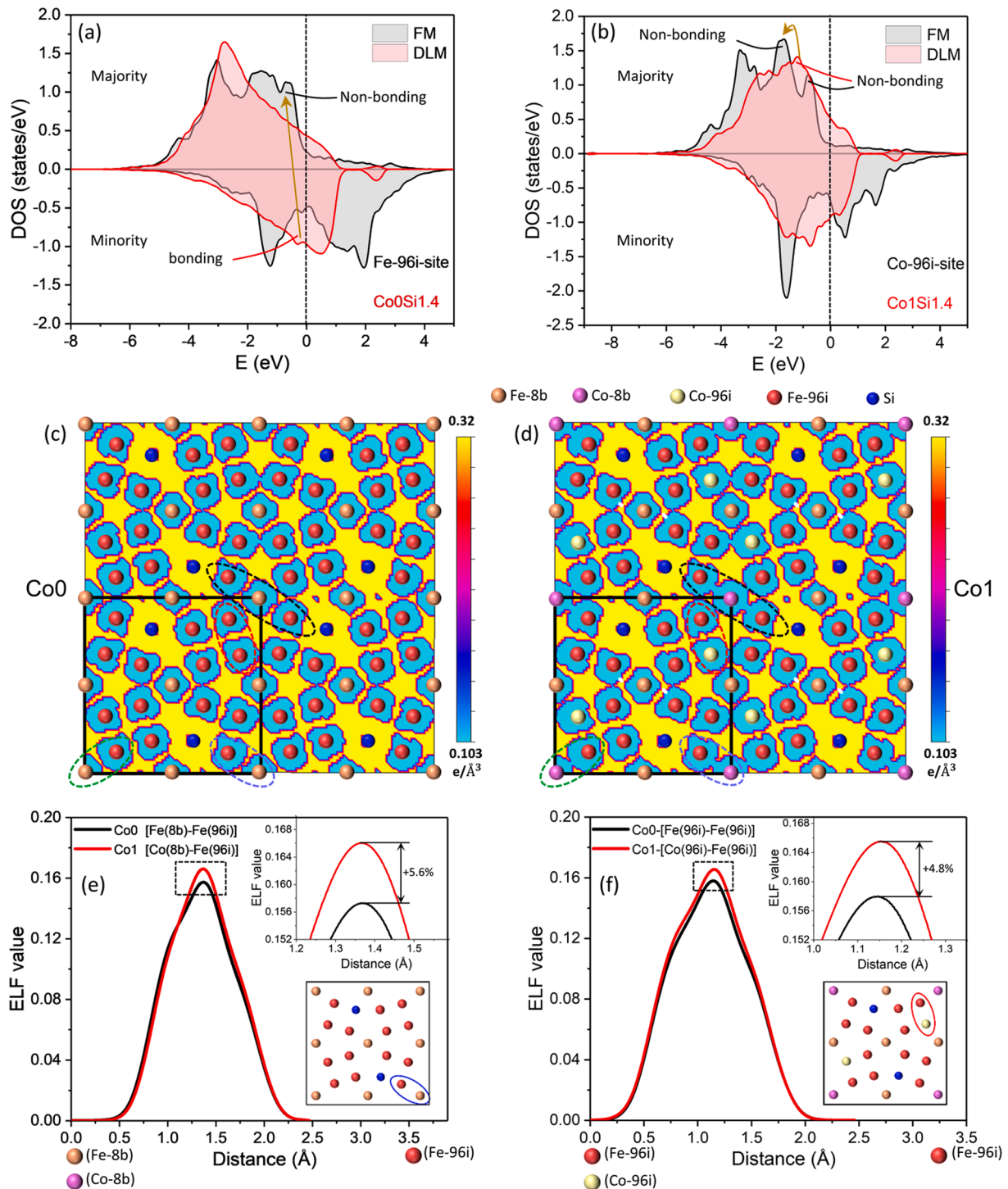
Fig. 4. (a) Atomic resolved contribution to density of state (DOS) of Fe atoms at 96i site for Co0; (b) Atomic resolved contribution to the DOS of Co atoms at 96i sites for Co1. The 2D electron localization function (ELF) maps of (c) Co0 and (d) Co1 parallel to the (001) surface, the range of ELF values is from 0.103 to 0.32, and the distance of the surface from the origin is set to be $1 \times d$, d is the inter-planar spacing. The images contain 2×2 unit cells, with the black box showing the range of individual cell. (e) Line profiles of the ELF values between Co(Fe)−8b and Fe-96i sites (blue circles in (c) and (d)). (f) Line profiles of the ELF values between Co(Fe)−96i and Fe-96i sites (red circles in (c) and (d)).

bonding electrons is increased after the entry of the Co atoms into the lattice. Hence, the lattice stress induced by magnetic order becomes smaller, namely, the weakened spontaneous magnetostriction, which effectively mitigated the lattice expansion upon strong magnetic ordering and eventually led to an extremely low thermal expansion in FM region for Co1. The above facts can be confirmed by the reduced magnetic moment which originates from the numbers of non-bonding electrons. According to the *ab initio* calculations, the average moments of magnetic atoms are 2.22 μ_B and 2.19 μ_B for Co0 and Co1, respectively, which is consistent with the experimentally measured saturated moments at 5 K (2.18 μ_B and 2.16 μ_B for Co0 and Co1 respectively, see the inset of Fig. 1a). Specifically, for Co1 (LaFe$_{10.6}$Co$_{1.0}$Si$_{1.4}$), the experimentally measured magnetic moment is basically consistent with that obtained by refining the NPD patterns at 5 K (2.08μ_B, SI-7, Figs. S8 and

S9). Further, the atomically resolved DOS curves of Fe 8b-site and Co 8b-site exhibit similar behaviors, as detailed in the supplementary information Fig. S7.

To further elucidate the role of Co atoms in regulating thermal expansion, we calculated the effective exchange coupling parameter J_{eff}. According to Weiss' theory, T_C is proportional to the effective coordination number z_{eff} times the renormalized exchange coupling parameter J_{eff} which implicitly includes the effects of the magnetic moments, namely, $T_C \sim z_{eff}J_{eff}$ [45]. Intriguingly, the calculated J_{eff} increases with Co doping, which is 36.021 meV and 38.878 meV for Co0 and Co1, respectively, suggesting more robust magnetic coupling in the Fe sub-lattice with Co cooperation against thermal fluctuation. According to the calculated J_{eff}, the increase of T_C is about 150 K based on $T_C \sim z_{eff}J_{eff}$, in line with the experimental observations from $T_C \sim 198$ K (Co0) to $T_C \sim 305$ K (Co1) by 107 K (Fig. 1a). A stronger exchange coupling suppresses the magnetic disorder induced by thermal fluctuations, which matches the M^2-T curves in Fig. 5c and d, i.e., a slower decrease rate in magnetization with temperature in FM region for Co1. Interestingly, this phenomenon also has a consistent counterpart in the V-T curve (Fig. 1d), i.e., a decrease in the slope of the V-T curve below T_C given the incorporation of Co.

Further, to verify the strengthening of the 3d metallic bonds mentioned above, the electron local function (ELF) has been calculated for the Co0 and Co1 samples. From the slice diagram that contains Fe/Co/Si atoms shown in Fig. 4c and d, the maximum value of ELF is about 0.319 for both Co0 and Co1 (see the color band on the left of each), representing the delocalization features of electrons among Fe, Co, Si atoms, which accords with the nature of metallic bonds (generally with ELF value < 0.5 [46]). Besides, from the 2D-ELF (Fig. 4c and d), one can see that the electron cloud appears "adhesion" between Fe and Co atoms (Co(8b)-Fe(96i), Co(96i)-Fe(96i)) in Co1 specimen (encircled by black, green, and blue circles in Fig. 4c and d), suggesting the modulation effect on the distribution of electrons by the doped Co atoms. Specifically, we extract the ELF curves between typical Fe, Co atoms. Fig. 4e shows that the ELF value between the Co-8b and Fe-96i increases by ~5.6% in Co1, as well as the 4.8% increase between the Co-96i and Fe-96i (Fig. 4f), which indicates a higher degree of electron localization between Fe and Co atoms. Moreover, it's worth noting that the five Fe-Fe bonds for Co1 are all shortened compared to these of Co0 from the 5 K XRD refinement, despite the fact that Fe and Co are adjacent in the periodic table of the elements, whose atomic radii are almost identical (Fig. S10). Therefore, we can draw the conclusion that the introduction of Co shortens the Fe (Co)-Fe(Co) distance and enhances the bonding strength, which not only stabilizes the low-temperature FM phase hence broadens FM region, but more importantly, the regulation of electron transfer and localization due to the introduction of Co also plays a vital role in improving the mechanical properties of materials, which benefits from the enhancement of the bonding strength.
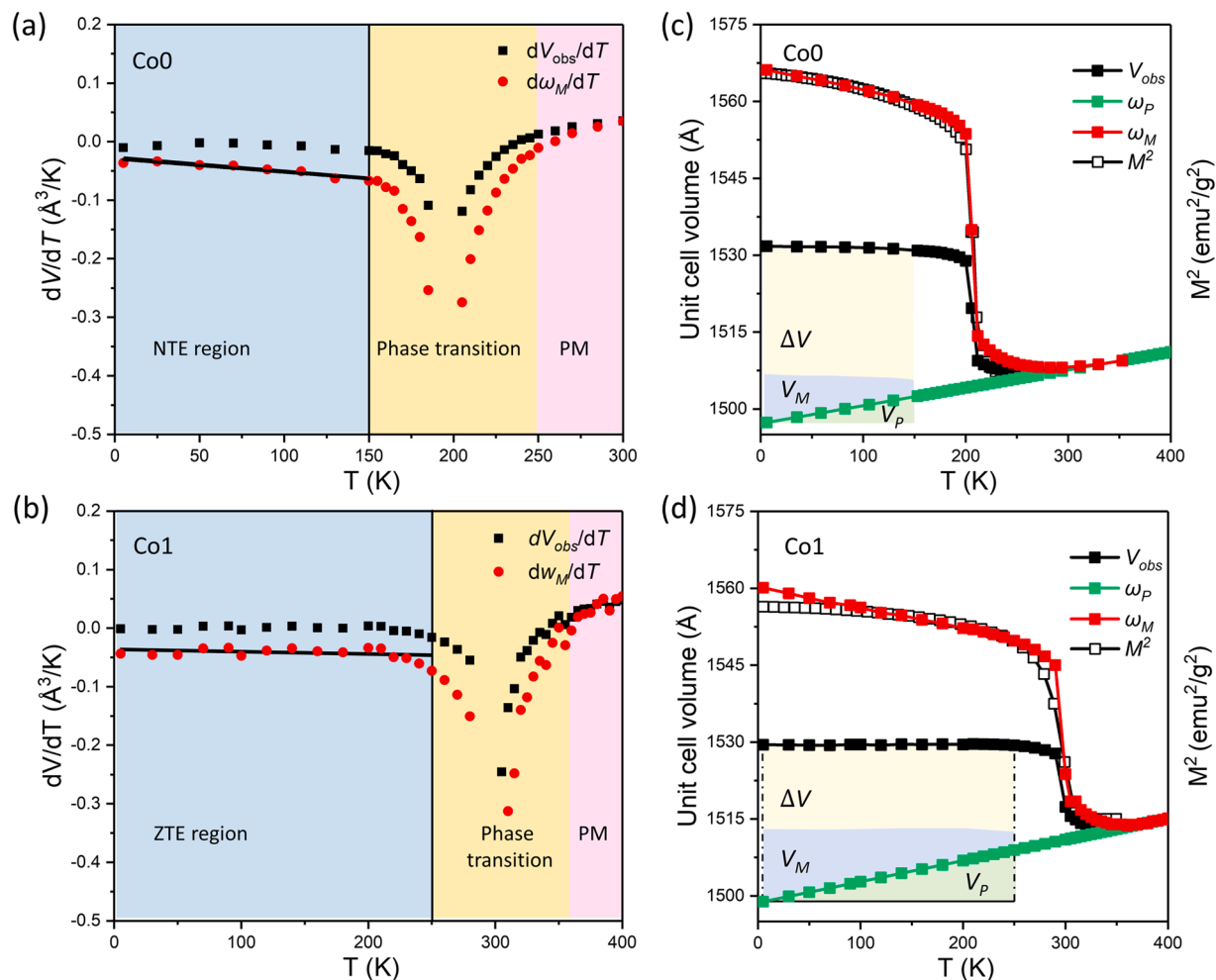

Fig. 5. The d$\omega_M(T)$/dT and dV_{obs}/dT as a function of temperature for (a) Co0, (b) Co1. Decomposed thermal expansion characteristics of LaFe$_{11.6-x}$Co$_x$Si$_{1.4}$ ($x = 0$, 1.0) (c) Co0 and (d) Co1. Where, the black, red line and green lines represent the evolution of the measured cell volume with temperature, the contribution of spontaneous magnetostriction and anharmonic lattice vibration, respectively. The relationship between the square of magnetization and temperature (yellow) is also given in (c) and (d).

3.4. Modulated magnetostriction

Since the thermal expansion behavior of magnetic material is closely relative to the spontaneous magnetostriction in the FM region, the volume of lattice can be expressed in the following form:

$$V_{obs}(T) = \omega_0 + \omega_P(T) + \omega_M(T)$$

where ω_0, $\omega_P(T)$, $\omega_M(T)$ are the unit cell volume in the ground state, the contribution of anharmonic lattice vibration (phonon term) and magnetic term (contribution of magnetic ordering), respectively. Since $\omega_M(T)$ is temperature independent above the Curie temperature, PTE comes from $\omega_P(T)$ that originated from the anharmonic lattice vibration subjected to Debye-Grüneisen relationship: $\omega_P = \gamma \frac{C_V k}{V_m}$, where γ and C_V are Grüneisen parameter and isochoric specific heat, $C_V = 3N_0 k_B$, k and V_m are isothermal compressibility ($k = -(1/V)(dV/dP)T$) and molar volume, respectively. The $\omega_M(T)$ was determined by $\omega_M(T) = V_{obs}(T) - \omega_P(T)$. Based on the previous studies [41,47], one would expect that the magneto-volume coupling scales linearly with the square of the magnetic moment below T_C, i.e., $\omega_M(T) = k \times M^2(T)$, where k is the constant of magneto-volume coupling, and $M(T)$ is the average moment of the magnetic atoms. In Fig. 5c and d we plot $M^2(T)$ as functions of temperature for both Co0 and Co1 in FM region. A similar trend for the extracted contribution ω_M and M^2 illustrated in Fig. 5c and d further demonstrates the close correlation between unit cell volume and magnetic ordering below T_C.

The change of unit cell volume in FM region can be attributed to the synergistic effect of the two factors $d\omega_M(T)/dT$ and $d\omega_P/dT$ with opposite signs. For Co0 compared to Co1, $d\omega_M(T)/dT$ changes a bit rapidly below T_C (Fig. 5a and b), leading to a rapid reduction of $\omega_M(T)$ upon heating and correspondingly a big change in unit cell volume. Since the

amplitude of $d\omega_M(T)/dT$ is larger than $d\omega_P/dT$, i.e., $-d\omega_M(T)/dT > d\omega_P/dT$, NTE behavior occurs in Co0 ($dV_{obs}/dT < 0$) below T_C. For Co1, $d\omega_M(T)/dT$ is adjusted to a relatively smaller rate that almost compensates the $d\omega_P/dT$ over a wide range of temperatures, i.e., $-d\omega_M(T)/dT \approx d\omega_P/dT$, hence a nearly temperature independent V, i.e., $dV_{obs}/dT = 0$ over 5–250 K interval below T_C, yielding an "ultra-wide" Invar form.

3.5. DOS near Fermi level and evolution of phase transition nature

The evolution of electronic structure with Co-doping and the origin of ZTE in Co1 have been analyzed above. The bonding electron transfer leads to increased effective exchange coupling parameter J_{eff} and suppressed spontaneous magnetostriction in FM region for Co1, which can also be confirmed by total DOS curves shown in Fig. 6a. With Co doping, the DOS curves of both spin up and spin down channel move to the low energy direction, implying the increase of electrons owe to more 3d electrons provided by Co atoms. Moreover, the increased number of spin down (6) is more than that of spin up (2), which explains the decrease of magnetic moment after Co doping in terms of electron transfer.

It should be noted that for La(Fe,Si)$_{13}$ alloy, the FM to PM phase transition brings a volume contraction about 1.0–1.6% [21]. There are two contributions to the experimental $V(T)$ besides $\omega_P(T)$, namely, the volume change of phase transition (ΔV) and the spontaneous magnetostriction in FM region (ω_M). During phase transition, the $\Delta V/V$ of Co1 (0.8%) is smaller than that of Co0 (1.2%), which can be attributed to the modulated phase transition nature and then the suppressed magneto-volume effect by Co introduction. The characteristics of nonmagnetic DOS can be used to discuss the order of FM-PM transition for the materials with strong magneto-volume and spin fluctuations [48]. Fig. 6b shows the nonmagnetic DOS of the two specimens. The effect of Co substitution on the FM-PM transition order in
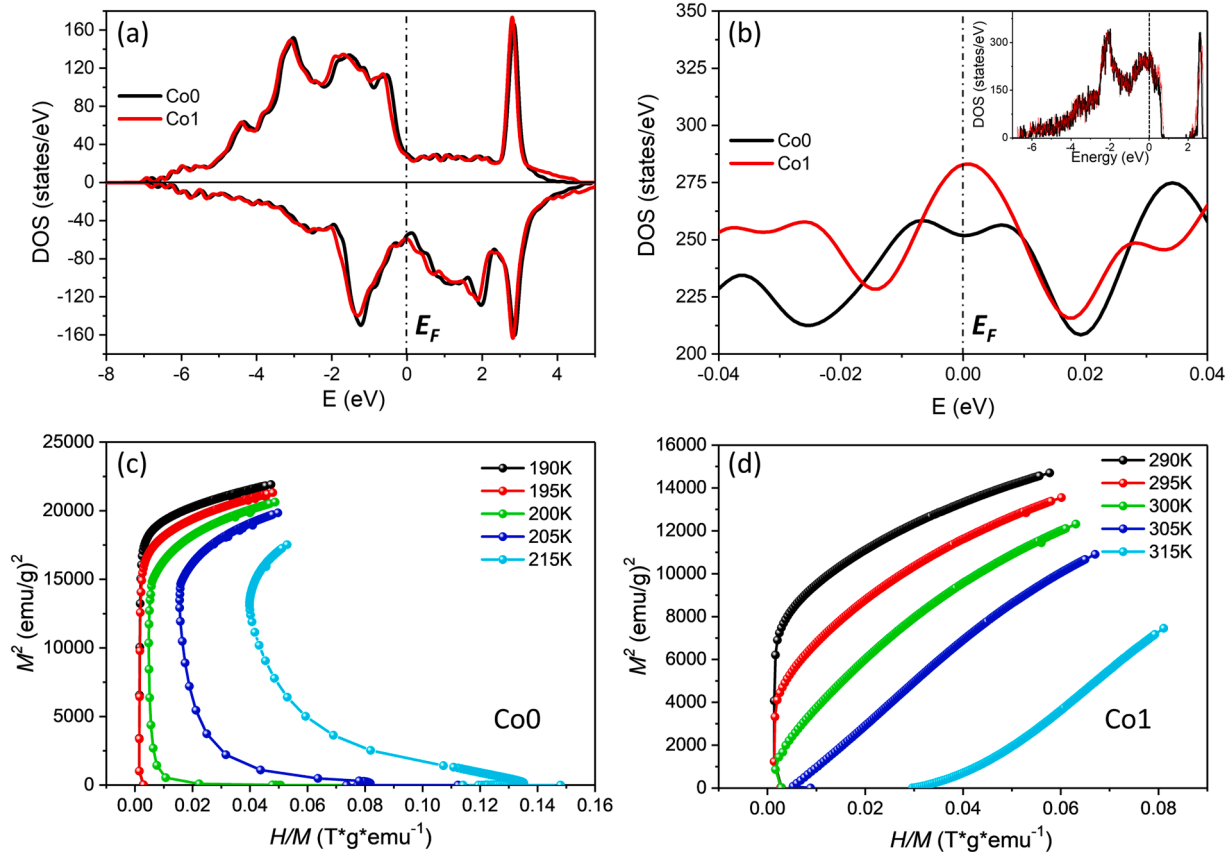

Fig. 6. (a) Total DOS at ferromagnetic state for Co0 and Co1. (b) Details of total DOS near the Fermi level E_F of the Co0 and Co1 in the nonmagnetic state, where the inset shows the total DOS in the nonmagnetic state. Arrott plots for (c) Co0 and (d) Co1.

LaFe$_{11.6-x}$Co$_x$Si$_{1.4}$ can be expressed in terms of the DOS behavior at the vicinity of E_F. In the Landau-Ginzburg expansion that includes the renormalization effect of spin fluctuations on the free energy $F(M)$, the mode-mode coupling coefficient b determines the order of the transition,

$$F(M) = \frac{1}{2}aM(T)^2 + \frac{1}{4}bM(T)^4 + \frac{1}{6}cM(T)^6 + \cdots - HM \qquad (1)$$

where a, b, and c can be calculated by using the DOS and their corresponding derivatives with respect to the energy at E_F. M and H represent the magnetization and magnetic field, respectively. The mode-mode coupling coefficient b can be expressed as follows,

$$b = \frac{1}{16\rho(E_F)^3}\left\{\left(\frac{\rho(E_F)'}{\rho(E_F)}\right)^2 - \frac{\rho(E_F)''}{3\rho(E_F)}\right\} \qquad (2)$$

where $\rho(E_F)$ represents the DOS at the Fermi level E_F of non-magnetic state. The sign for b is related to the curvature of DOS at the Fermi level, and reflects the order of phase transitions. The induced changes by Co doping in DOS curvature can be clearly identified in Fig. 6b that the Fermi levels locate at the minima and maxima for Co0 and Co1 respectively. According to Eq. (2), the calculated b for Co0 is $b = -2.81 \times 10^{-6}$, which becomes $b = 3.29 \times 10^{-6}$ when Co atoms are introduced (Co1). The sign of b changes from negative to positive, illustrating an evolution from FOPT to SOPT by Co doping. This theoretical result agrees well with the experimentally constructed Arrott plots (Fig. 6c and d) according to Banerjee's criterion. All these explain the suppressed magneto-volume effect involving the SOPT by Co substitution.

3.6. Critical behavior and magnetocaloric effects

Due to the substitution of Co, the electronic structure of LaFe$_{11.6-x}$Co$_x$Si$_{1.4}$ has been significantly changed, and the influence on magnetism and lattice is not only reflected in the FM region, but also in the phase transition interval, which brings a series of changes on critical behaviors of phase transition and physical properties.

To investigate the influence of the evolution of electronic structure on the magnetocaloric effect, isothermal magnetic entropy changes ΔS_M were calculated according to the Maxwell thermodynamic relation and the measured M-H data (Fig. 7a and b). Generally, giant ΔS_M results from the simultaneously drastic change of lattice and magnetization. For Co0, ΔS reaches 28.6 J·kg^{-1}·K^{-1} under $\Delta\mu_0H = 2$ T, exhibiting giant MCE. Moreover, the ΔS_M-T curves broaden asymmetrically toward high temperature with increased $\Delta\mu_0H$, which is primarily caused by itinerant electron metamagnetic transition above T$_C$. While for Co1, ΔS_M is 7.1 J·kg^{-1}·K^{-1} under $\Delta\mu_0H = 2$ T. One can note the following three points for Co1: (I) The magnitude of ΔS_M decreases by more than 50% compared to Co0 under any $\Delta\mu_0H$, (II) The ΔS_M curves are almost bell-shaped and nearly axisymmetric. (III) The driving capacity of magnetic field on the peak temperature of ΔS_M, i.e., dT/dH, decreases from 1.3 K/T for Co0 to 0.3 K/T for Co1. All these indicate that with Co-doping, magneto-volume coupling is inhibited, consistent with the reduced volume change observed in the phase transition interval of Co1. In addition, the relative cooling power (RCP), expressed by Eq. (3), [24,49] allows us to assess the energy that can be transferred between the cold and hot ends in an ideal magnetic refrigeration cycle:
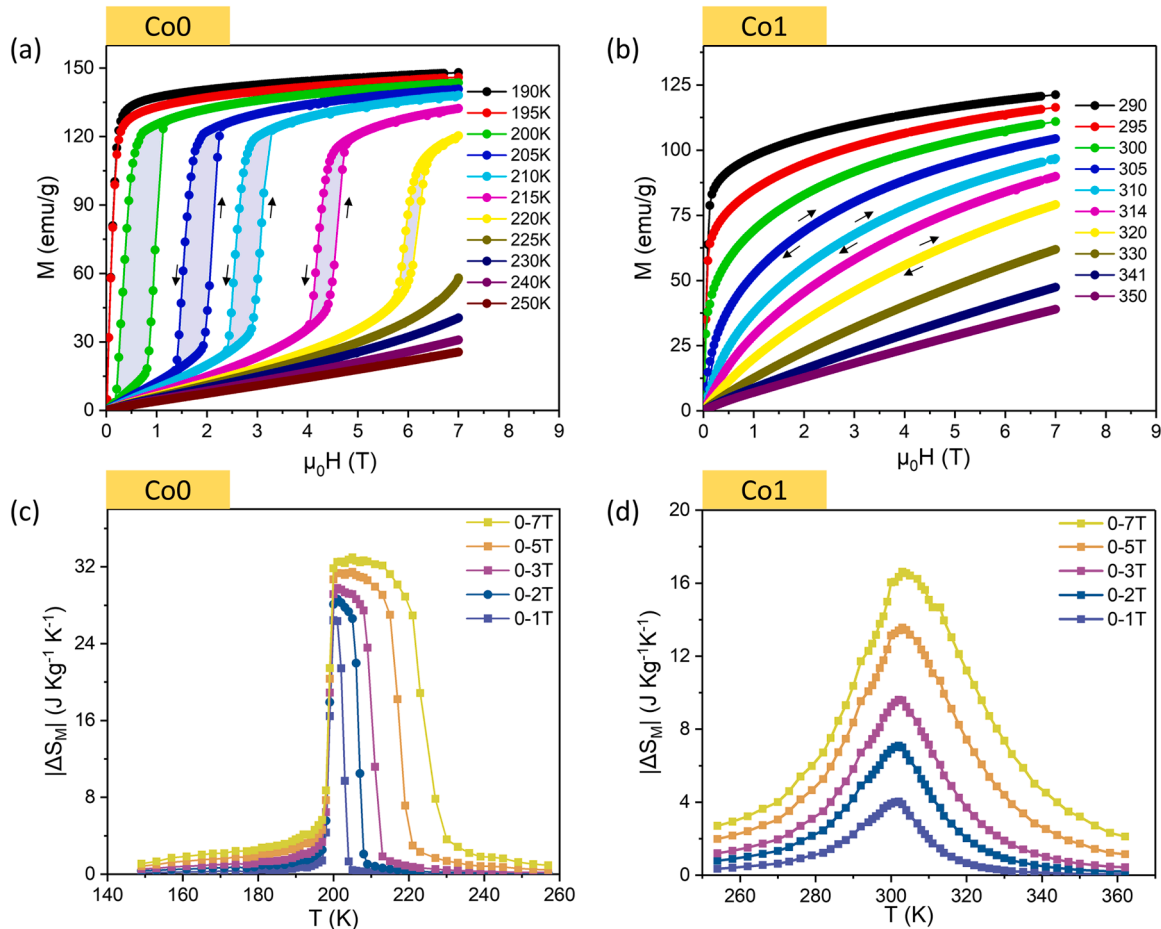

Fig. 7. Isothermal magnetization curves (M-H) of (a) Co0 and (b) Co1 at selected temperatures near T$_C$. Isothermal magnetic entropy changes (ΔS_M) for (c) Co0 and (d) Co1.

$$RCP = \left|\Delta S_M^{max}\right| \times \delta T_{FWHM} \tag{3}$$

Co0 undergoing FOPT shows stronger cooling capacity, and the RCP reaches 104.0 J·kg^{-1} at $\mu_0 H = 1$ T and 832.9 J·kg^{-1} at $\mu_0 H = 7$ T, both of which are higher than corresponding values of Co1 (Fig. 8a, 86.1 J·kg^{-1} at $\mu_0 H = 1$ T and 690.0 J·kg^{-1} at $\mu_0 H = 7$ T). However, the presence of magnetic/thermal hysteresis reduces the cooling efficiency and even disrupts the thermal dynamic cycle. The maximum hysteretic loss of Co0 during the magnetization-demagnetization cycle is calculated to be 66.5 J·kg^{-1}, while the hysteresis loss of Co1 approaches zero. After deducting the influence of hysteresis loss, the reversible RCP are shown in Fig. 8b. Given low magnetic field change ($\mu_0 H = 2$ T) easily accessed by permanent magnet, the reversible RCP of Co1 is 183.6 J·kg^{-1}, 13.7% higher than that of Co0 (Fig. 8b, about 161.5 J·kg^{-1}). Although RCP is reduced by Co doping, reversible RCP is increased due to elimination of hysteresis, suggesting that the LaFe$_{10.6}$Co$_{1.0}$Si$_{1.4}$ with excellent mechanical property possesses advantages as a promising candidate for room temperature magnetic refrigerant (Table S5).

Based on the magnetic field dependence of ΔS_M, we quantified the influence of electronic structure changes on the critical behavior of phase transition, and the following equation about n exponent is adopted [50]:

$$n(T,H) = \frac{d\ln|\Delta S_M|}{d\ln H} \tag{4}$$

According to the temperature dependence of n exponent for SOPT materials [50,51], at temperatures well below T_C, n should have a value that tends to 1; for temperatures far higher than T_C, n tends to the paramagnetic value of 2, while for the temperatures around T_C, n has a value that depends on the critical exponents of the material, provided that the applied magnetic field is in the range that make the material remain within the critical region. For Co1, we find a trend of n exponent from 1 → minimum → 2 in the $n(T)$ isofield curves (Fig. 8d). However,

the behavior is dissimilar for specimen Co0. Although the low and high temperature limits ($n = 1$ and $n = 2$, respectively) are still observed, the minimum of n exponent is closely followed by its maximum significantly larger than 2 with increasing temperature, and the maximum behaves field dependent (Fig. 8c). Such a overshoot of n exponent above 2 is a distinctive feature of FOPT [50]. For a FOPT sample, a discontinuous change of entropy (ΔS_M) occurs, giving rise to a latent heat $\Delta Q = T_C \times \Delta S$ at the critical temperature owe to strong magneto-volume coupling (Co0), which is witnessed by a sudden jump in the value of n above T_C. While for Co1, the n value slowly transforms from 1 in FM state to 2 in PM state, which strongly indicates the weakening of magneto-volume coupling by Co doping.

4. Conclusions

In summary, Invar effect with excellent mechanical property has been demonstrated in LaFe$_{11.6-x}$Co$_x$Si$_{1.4}$ magnetocaloric materials by electronic structure modulation via Co doing. In La(Fe,Si,Co)$_{13}$ with NaZn$_{13}$-type structure, the 3 elements of Fe, Si, Co all occupy two crystallographic positions, i.e. FeI (8b) and FeII (96i). By taking advantage of distinct resolution ability of neutrons and X-rays to Fe/Co adjacent elements, the occupancy of Co atoms was determined, for the first time, by utilizing a joint refinement strategy of NPD and XRD, despite over 20 years of attention focused on this material family for MCE. On the basis, *ab initio* calculations were performed on the atomically resolved electronic band structure. The results demonstrated that the incorporation of Co atoms alters the electron transfer properties by increasing 3d bonding electrons at Co sub-lattice, which inhibits the spontaneous magnetostriction and weakens the lattice stress compared to the LaFe$_{11.6}$Si$_{1.4}$ without Co. The balance between the suppressed negative contribution of magnetostriction and the general positive expansion caused by anharmonic lattice vibration leads to Invar effect
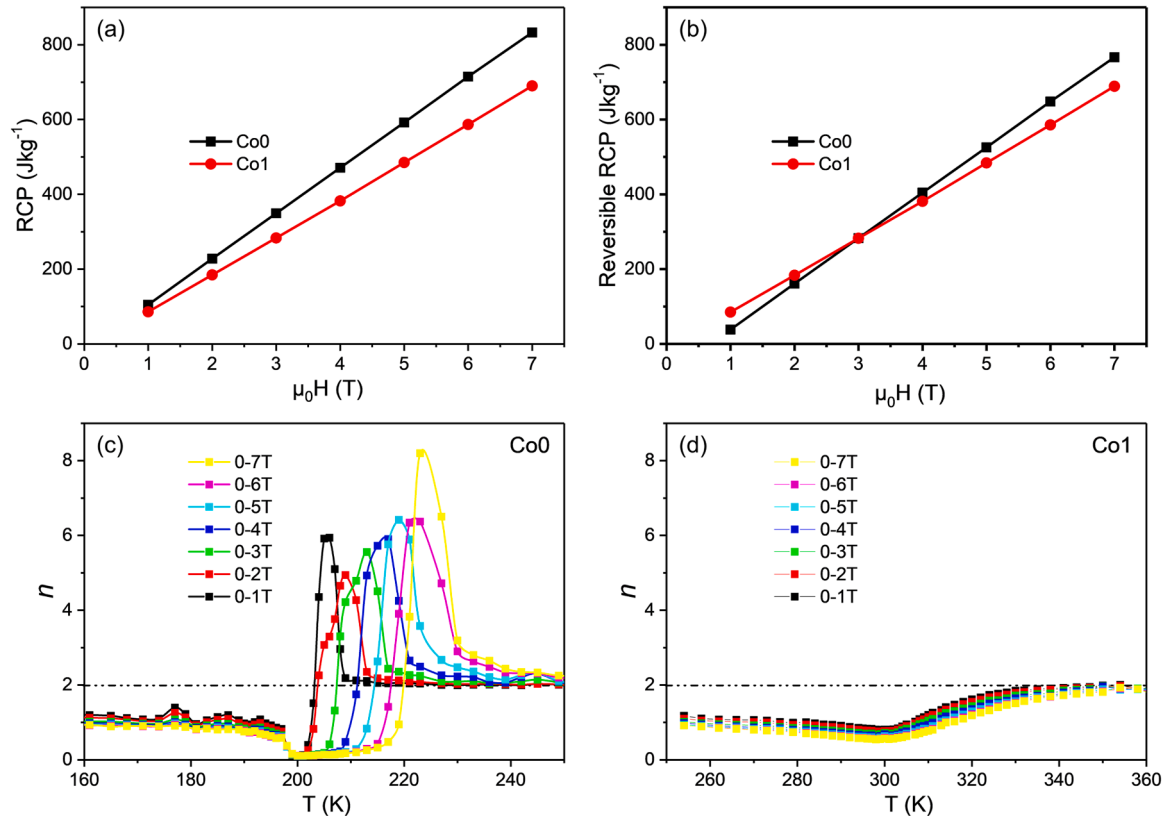

Fig. 8. (a) RCP and (b) reversible RCP against magnetic field change $\Delta\mu_0 H$ for Co0 and Co1. Field and temperature dependence of the exponent n for (c) Co0 and (d) Co1. The values of $n > 2$ for Co0 clearly indicate its FOPT behavior, while Co1 is a SOPT.

over a wide temperature interval in the ferromagnetic region of $LaFe_{10.6}Co_{1.0}Si_{1.4}$. The observed linear thermal expansion coefficient ($\alpha_l \sim 1.5 \times 10^{-8}\,K^{-1}$, $\Delta T = 5$–$250\,K$, by XRD; $\alpha_l \sim 2.7 \times 10^{-7}\,K^{-1}$, 109–250 K, by dilatometer) is better than most other ZTE materials including the famous Invar alloy $Fe_{0.65}Ni_{0.35}$. Moreover, calculations of ELF confirmed the enhanced metallic bonding due to more localized electrons between Fe and Co (Co(8b)-Fe(96i), Co(96i)-Fe(96i)) and thereby improved mechanical properties upon Co doping. The measured compressive strength up to ~ 340 MPa makes the $LaFe_{10.6}Co_{1.0}Si_{1.4}$ suitable for machining purposes.

Further, the correlation of electronic structure with phase transition nature was studied in detail. The mode-mode coupling coefficient *b* calculated from density of states explain the evolution of phase transition from first-order to second-order upon Co doping, which gives $LaFe_{10.6}Co_{1.0}Si_{1.4}$ a significant advantage in its effective cooling capacity under a low magnetic field accessed by permanent magnets. These findings pave a way for tailoring multifunctional properties of $La(Fe,Co,Si)_{13}$, a known family for MCE, by electronic structure modulation.

Declaration of Competing Interest

The authors declare that they have no known competing financial interests or personal relationships that could have appeared to influence the work reported in this paper.

Acknowledgments

Supplementary materials

Supplementary material associated with this article can be found, in the online version, at doi:10.1016/j.actamat.2023.119312.

References

[1] A.L. Goodwin, M. Calleja, M.J. Conterio, M.T. Dove, J.S.O. Evans, D.A. Keen, L. Peters, M.G. Tucker, Colossal positive and negative thermal expansion in the framework material $Ag_3Co(CN)_6$, Science 319 (5864) (2008) 794–797.

[2] J.P. Attfield, A fresh twist on shrinking materials, Nature 480 (7378) (2011) 465–466.

[3] T.A. Mary, J.S.O. Evans, T. Vogt, A.W. Sleight, Negative thermal expansion from 0.3 to 1050 K in ZrW_2O_8, Science 272 (5258) (1996) 90–92.

[4] J. Chen, X. Xing, C. Sun, P. Hu, R. Yu, X. Wang, L. Li, Zero thermal expansion in $PbTiO_3$-based perovskites, J. Am. Chem. Soc. 130 (4) (2008) 1144–1145.

[5] X.G. Zheng, H. Kubozono, H. Yamada, K. Kato, Y. Ishiwata, C.N. Xu, Giant negative thermal expansion in magnetic nanocrystals, Nat. Nanotechnol. 3 (12) (2008) 724–726.

[6] Y.W. Long, N. Hayashi, T. Saito, M. Azuma, S. Muranaka, Y. Shimakawa, Temperature-induced A-B intersite charge transfer in an A-site-ordered $LaCu_3Fe_4O_{12}$ perovskite, Nature 458 (7234) (2009), 60-U3.

[7] M. Azuma, W.T. Chen, H. Seki, M. Czapski, S. Olga, K. Oka, M. Mizumaki, T. Watanuki, N. Ishimatsu, N. Kawamura, S. Ishiwata, M.G. Tucker, Y. Shimakawa, J.P. Attfield, Colossal negative thermal expansion in $BiNiO_3$ induced by intermetallic charge transfer, Nat. Commun. 2 (2011) 347.

[8] C.W. Li, X. Tang, J.A. Munoz, J.B. Keith, S.J. Tracy, D.L. Abernathy, B. Fultz, Structural relationship between negative thermal expansion and quartic anharmonicity of cubic ScF_3, Phys. Rev. Lett. 107 (19) (2011), 195504.

[9] F. Hu, F. Shen, J. Hao, Y. Liu, J. Wang, J. Sun, B. Shen, Negative thermal expansion in the materials with giant magnetocaloric effect, Front. Chem. 6 (2018) 438.

[10] Y. Cao, K. Lin, S. Khmelevskyi, M. Avdeev, K.M. Taddei, Q. Zhang, Q. Huang, Q. Li, K. Kato, C.C. Tang, A. Gibbs, C.W. Wang, J. Deng, J. Chen, H. Zhang, X. Xing, Ultrawide temperature range super-Invar behavior of $R_2(Fe,Co)_{17}$ materials (R = Rare Earth), Phys. Rev. Lett. 127 (5) (2021), 055501.

[11] Y. Sun, C. Wang, Q. Huang, Y. Guo, L. Chu, M. Arai, K. Yamaura, Neutron diffraction study of unusual phase separation in the antiperovskite nitride Mn_3ZnN, Inorg. Chem. 51 (13) (2012) 7232–7236.

[12] X.G. Guo, J.C. Lin, P. Tong, M. Wang, Y. Wu, C. Yang, B. Song, S. Lin, W.H. Song, Y. P. Sun, Magnetically driven negative thermal expansion in antiperovskite $Ga_{1-x}Mn_xN_{0.8}Mn_3$ ($0.1 <= x <= 0.3$), Appl. Phys. Lett. 107 (20) (2015), 202406.

[13] R. Huang, Y. Liu, W. Fan, J. Tan, F. Xiao, L. Qian, L. Li, Giant negative thermal expansion in NaZn13-Type $La(Fe, Si, Co)_{13}$ compounds, J. Am. Chem. Soc. 135 (31) (2013) 11469–11472.

[14] S.E. Tallentire, F. Child, I. Fall, L. Vella-Zarb, I.R. Evans, M.G. Tucker, D.A. Keen, C. Wilson, J.S.O. Evans, Systematic and controllable negative, zero, and positive thermal expansion in cubic $Zr_{1-x}Sn_xMo_2O_8$, J. Am. Chem. Soc. 135 (34) (2013) 12849–12856.

[15] C.É. Guillaume, Recherches sur les aciers auch nickel, Gauthier-Villars 125 (1897) 18.

[16] J.R. Salvador, F. Gu, T. Hogan, M.G. Kanatzidis, Zero thermal expansion in YbGaGe due to an electronic valence transition, Nature 425 (6959) (2003) 702–705.

[17] J. Liu, B. Ding, Y. Yao, X. Xi, Z. Cheng, J. Wang, C.-w. Wang, G. Wu, W. Wang, Coherent spin rotation-induced zero thermal expansion in MnCoSi-based spiral magnets, NPG Asia Mater. 13 (1) (2021) 70.

[18] C. Yu, K. Lin, S. Jiang, Y. Cao, W. Li, Y. Wang, Y. Chen, K. An, L. You, K. Kato, Q. Li, J. Chen, J. Deng, X. Xing, Plastic and low-cost axial zero thermal expansion alloy by a natural dual-phase composite, Nat. Commun. 12 (2021) 4701.

[19] J. Xu, Z. Wang, H. Huang, Z. Li, X. Chi, D. Wang, J. Zhang, X. Zheng, J. Shen, W. Zhou, Y. Gao, J. Cai, T. Zhao, S. Wang, Y. Zhang, B. Shen, Significant zero thermal expansion via enhanced magnetoelastic coupling in Kagome magnets, Adv. Mater. 35 (8) (2023), 2208635.

[20] K.A. Gschneidner, V.K. Pecharsky, A.O. Tsokol, Recent developments in magnetocaloric materials, Rep. Prog. Phys. 68 (6) (2005) 1479–1539.

[21] B.G. Shen, J.R. Sun, F.X. Hu, H.W. Zhang, Z.H. Cheng, Recent progress in exploring magnetocaloric materials, Adv. Mater. 21 (45) (2009) 4545–4564.

[22] O. Gutfleisch, M.A. Willard, E. Bruck, C.H. Chen, S.G. Sankar, J.P. Liu, Magnetic materials and devices for the 21st century: stronger, lighter, and more energy efficient, Adv. Mater. 23 (7) (2011) 821–842.

[23] X. Moya, S. Kar-Narayan, N.D. Mathur, Caloric materials near ferroic phase transitions, Nat. Mater. 13 (5) (2014) 439–450.

[24] V. Franco, J.S. Blazquez, J.J. Ipus, J.Y. Law, L.M. Moreno-Ramirez, A. Conde, Magnetocaloric effect: from materials research to refrigeration devices, Prog. Mater Sci. 93 (2018) 112–232.

[25] F.X. Hu, B.G. Shen, J.R. Sun, Z.H. Cheng, G.H. Rao, X.X. Zhang, Influence of negative lattice expansion and metamagnetic transition on magnetic entropy change in the compound $LaFe_{11.4}Si_{1.6}$, Appl. Phys. Lett. 78 (23) (2001) 3675–3677.

[26] K. Engelbrecht, C.R.H. Bahl, K.K. Nielsen, Experimental results for a magnetic refrigerator using three different types of magnetocaloric material regenerators, Int. J. Refrig. 34 (4) (2011) 1132–1140.

[27] A. Funk, J. Freudenberger, A. Waske, M. Krautz, Getting magnetocaloric materials into good shape: cold-working of $La(Fe, Co, Si)_{13}$ by powder-in-tube-processing, Mater. Today Energy 9 (2018) 223–228.

[28] S. Li, R. Huang, Y. Zhao, W. Wang, Y. Han, L. Li, Zero thermal expansion achieved by an electrolytic hydriding method in $La(Fe, Si)_{13}$ compounds, Adv. Funct. Mater. 27 (5) (2017), 1604195.

[29] J. Chen, L. Hu, J. Deng, X. Xing, Negative thermal expansion in functional materials: controllable thermal expansion by chemical modifications, Chem. Soc. Rev. 44 (11) (2015) 3522–3567.

[30] P. Hartmann, R. Jedamzik, A. Carre, J. Krieg, T. Westerhoff, Glass ceramic ZERODUR (R): even closer to zero thermal expansion: a review, part 1, J. Astron. Telesc. Instrum. Syst. 7 (2) (2021), 020901.

[31] B.A. Marinkovic, P.I. Ponton, C.P. Romao, T. Moreira, M.A. White, Negative and near-zero thermal expansion in $A_2M_3O_{12}$ and related ceramic families: a review, Front. Mater. 8 (2021) 741560.

[32] J. Dawidowski, J.R. Granada, J.R. Santisteban, F. Cantargi, L. Palomino, Neutron scattering lengths and cross sections, Exp. Methods Phys. Sci. 44 (2013) 471–528.

[33] L. He, S. Deng, F. Shen, J. Chen, H. Lu, Z. Tan, H. Zheng, J. Hao, D. Zhao, Q. Ma, The performance of general purpose powder diffractometer at CSNS, Nucl. Instrum. Meth. A 1054 (2023), 168414.

[34] G. Kresse, J. Furthmuller, Efficient iterative schemes for *ab initio* total-energy calculations using a plane-wave basis set, Phys. Rev. B 54 (16) (1996) 11169–11186.

[35] P.E. Blochl, Projector augmented-wave method, Phys. Rev. B 50 (24) (1994) 17953–17979.

[36] B. Hammer, L.B. Hansen, J.K. Norskov, Improved adsorption energetics within density-functional theory using revised Perdew-Burke-Ernzerhof functionals, Phys. Rev. B 59 (11) (1999) 7413–7421.

[37] R.B. Helmholdt, T.T.M. Palstra, G.J. Nieuwenhuys, J.A. Mydosh, A. M. Vanderkraan, K.H.J. Buschow, Magnetic-properties of $La(Fe_xAl_{1-x})_{13}$ determined via neutron-scattering and mossbauer-spectroscopy, Phys. Rev. B 34 (1) (1986) 169–173.

[38] H. Chang, N.X. Chen, J.K. Liang, G.G. Rao, Theoretical study of phase forming of NaZn13-type rare-earth intermetallics, J. Phys. Condens. Matter. 15 (2) (2003) 109–120.

[39] F. Wang, A. Kurbakov, G.J. Wang, F.X. Hu, B.G. Shen, Z.H. Cheng, Strong interplay between structure and magnetism in $LaFe_{11.3}Co_{0.6}Si_{1.1}$: a neutron diffraction study, Physica B 385 (2006) 343–345.

[40] A. Fujita, H. Yako, Stability of metallic, magnetic and electronic states in NaZn13-type $La(Fe_xSi_{1-x})_{13}$ magnetocaloric compounds, Scripta Mater. 67 (6) (2012) 578–583.

[41] S. Khmelevskyi, P. Mohn, Magnetostriction in Fe-based alloys and the origin of the Invar anomaly, Phys. Rev. B 69 (14) (2004), 140404(R).

[42] S. Khmelevskyi, I. Turek, P. Mohn, Large negative magnetic contribution to the thermal expansion in iron-platinum alloys: quantitative theory of the Invar effect, Phys. Rev. Lett. 91 (3) (2003), 037201.

[43] X.H. Kang, J.M. Zhang, The structural, electronic and magnetic properties of a novel quaternary Heusler alloy TiZrCoSn, J. Phys. Chem. Solids 105 (2017) 9–15.

[44] K. Takenaka, Progress of research in negative thermal expansion materials: paradigm shift in the control of thermal expansion, Front. Chem. 6 (2018) 267.

[45] J.T. Wang, L. Zhou, D.S. Wang, Y. Kawazoe, Exchange interaction and magnetic phase transition in layered Fe/Au(001) superlattices, Phys. Rev. B 62 (2000) 3354.

[46] B. Silvi, A. Savin, Classification of chemical bonds based on topological analysis of electron localization functions, Nature 371 (1994) 683–686.

[47] Y. Kakehashi, A theory of the magnetovolume effect at finite temperatures, J. Phys. Soc. Jpn. 50 (6) (1981) 1925–1933.

[48] A. Fujita, K. Fukamichi, J.T. Wang, Y. Kawazoe, Large magnetovolume effects and band structure of itinerant-electron metamagnetic $La(Fe_xSi_{1-x})_{13}$ compounds, Phys. Rev. B 68 (10) (2003), 104431.

[49] Y. Zhang, Y. Tian, Z. Zhang, Y. Jia, B. Zhang, M. Jiang, J. Wang, Z. Ren, Magnetic properties and giant cryogenic magnetocaloric effect in B-site ordered antiferromagnetic Gd_2MgTiO_6 double perovskite oxide, Acta Mater 226 (2022), 117669.

[50] J. Yan Law, V. Franco, L. Miguel Moreno-Ramirez, A. Conde, D.Y. Karpenkov, I. Radulov, K.P. Skokov, O. Gutfleisch, A quantitative criterion for determining the order of magnetic phase transitions using the magnetocaloric effect, Nat. Commun. 9 (2018) 2680.

[51] V. Franco, J.S. Blazquez, A. Conde, Field dependence of the magnetocaloric effect in materials with a second order phase transition: a master curve for the magnetic entropy change, Appl. Phys. Lett. 89 (22) (2006), 222512.